Front. Energy 2025, 19(6): 999–1006
https://doi.org/10.1007/s11708-025-1015-3

RESEARCH ARTICLE

Formamide-engineered $VOPO_4$ cathodes with high volumetric capacity and mass loading for aqueous zinc-ion batteries

Yueyue Li[1], Tao Li[2], Yi Shen[2], ShuhuaYang [1], Kui Li (✉)[1], Tianquan Lin (✉)[2]

1 School of Materials Science and Engineering, University of Jinan, Jinan 250022, China
2 School of Materials Science and Engineering, Zhangjiang Institute for Advanced Study (ZIAS), Shanghai Jiao Tong University, Shanghai 200240, China

Abstract Aqueous zinc-ion batteries (AZIBs) have emerged as promising candidates for next-generation energy storage systems due to their inherent safety, cost-effectiveness, and high theoretical capacity. However, their practical application remains constrained by limited cycling stability and sluggish ion diffusion kinetics, particularly under high mass loading conditions. These limitations are primarily attributed to the restricted ion transport pathways within the electrode structure and structural degradation caused by repeated zinc-ion insertion and extraction in highly loaded electrodes. To address these challenges, formamide (FA)-inserted $VOPO_4$ (FA-$VOPO_4$) nanosheet cathodes were designed with expanded interlayer spacing (9.3 Å), where FA molecules partially replace interlayer water, thereby enhancing both structural stability and ion transport pathways. This unique structural modification, supported by synergistic hydrogen bonding between FA and residual water, significantly improves Zn^{2+} diffusion kinetics and charge transfer properties, as confirmed by electrochemical tests and theoretical analysis. Consequently, FA-$VOPO_4$ electrodes delivered a remarkable volumetric capacity of 733 mAh/cm^3 at 40 mA/g, approximately 8 times higher than that of the $VOPO_4{\cdot}2H_2O$ electrode, and retained 82.1% of their capacity after 1000 cycles at 1 A/g with a mass loading of 10 mg/cm^2. Even at a high mass loading of 20 mg/cm^2 (4.4 mAh/cm^2), the FA-$VOPO_4$ cathode maintained a volumetric capacity of 535 mAh/cm^3. These findings provide valuable insights into electrode design strategies for high-performance AZIBs, contributing to the development of safer, more efficient energy storage technologies with potential applications in grid storage and portable electronics.

Keywords high mass loading, aqueous zinc-ion battery, high volumetric capacity, FA-$VOPO_4$

1 Introduction

Aqueous zinc-ion batteries (AZIBs) are gaining attention as promising energy storage solutions for grid applications and flexible wearable devices due to zinc's favorable properties [1], including a low redox potential (−0.763 V versus standard hydrogen electrode), high theoretical volumetric capacity (5851 mAh/cm^3), cost-effectiveness, environmental compatibility, and intrinsic safety [2–5]. Paired with suitable cathode materials, AZIBs can achieve competitive energy densities. However, existing cathode materials, such as manganese-based compounds [6,7], Prussian blue analogs [8,9], and vanadium-based compounds [10,11], face substantial challenges, including structural degradation, capacity fading, and poor cycling stability. These limitations are further exacerbated under high mass loading conditions, which are essential for improving energy density but hindered by low conductivity, sluggish reaction kinetics, and poor interfacial stability with aqueous electrolytes [3,12,13]. Furthermore, the limited specific capacity of cathode materials under high mass loading reduces the overall volumetric energy storage potential, preventing full utilization of the high volumetric capacity of the zinc anode.

Achieving high-performance cathodes under high mass

Received Jan. 24, 2025; accepted Apr. 11, 2025; online Jun. 10, 2025
Correspondences: Kui Li, mse_lik@ujn.edu.cn;
Tianquan Lin, tqlin@sjtu.edu.cn

loading conditions requires a combination of structural robustness, high electronic and ionic conductivity, and fast reaction kinetics. Ideal cathode materials should enable efficient zinc-ion insertion and extraction while maintaining structural integrity throughout extended cycling [14–17]. Layered vanadium-based compounds, such as $VOPO_4$, stand out due to their open frameworks and tunable interlayer spacing, which facilitate rapid ion transport [10,18–21]. Among these, $VOPO_4$ has emerged as a promising candidate due to its high theoretical capacity (over 300 mAh/g) and superior reaction kinetics [22–25]. However, its practical application in AZIBs is impeded by several critical challenges: the high charge-to-size ratio of zinc ions leads to significant electrostatic repulsion, causing lattice expansion and structural degradation [26,27]. Additionally, $VOPO_4$ tends to irreversibly transform into less active phases, such as VO_x, resulting in rapid capacity decay and reduced cycle life [28–30].

To address these challenges, various interlayer engineering strategies have been explored, including expanding interlayer spacing via self-assembled organic molecules, to enhance the electrochemical performance of $VOPO_4$ cathodes in zinc-ion batteries [22,31,32]. Additionally, interlayer cation pre-intercalation (Li^+, Na^+, K^+, NH_4^+, Cu^{2+}, etc.) has also been employed to enlarge interlayer distance and reduce electrostatic interactions between inserted Zn^{2+} and the crystal framework, significantly improving Zn^{2+} diffusion kinetics [33–37]. Another approach involves introducing water molecules to form $VOPO_4{\cdot}2H_2O$, where interlayer water molecules alleviate electrostatic repulsion and mitigate volumetric changes during cycling, thereby enhancing capacity and stability [38]. However, under high mass loading conditions, this approach has proven insufficient due to sluggish ion diffusion and limited electronic conductivity. The ion diffusion pathways may lack the speed and interconnectivity to accommodate the large flux of Zn^{2+} ions required under high mass loading. This results in sluggish ion diffusion kinetics, particularly in thick electrodes, where deeper layers become less accessible [39]. While water molecules increase interlayer spacing to facilitate zinc-ion insertion and extraction, they also strongly hydrate the zinc ions, reducing their mobility and slowing ion diffusion kinetics [40–42]. This issue becomes particularly pronounced in thick electrodes, ultimately limiting the electrochemical performance of $VOPO_4{\cdot}2H_2O$.

In this study, a novel strategy is proposed to overcome these limitations by intercalating formamide (FA) instead of water into the $VOPO_4$ interlayer. FA shares many physical and molecular-structural properties with water but offers high donor number (DN), which quantifies the solvent's ability to donate electron pairs or act as a Lewis base (refer to Table S1 for details). This property enables FA to establish moderate interactions with Zn^{2+} ions while enhancing their mobility. The intercalation of FA increases the interlayer spacing of $VOPO_4$, facilitating easier zinc-ion insertion and extraction, while also improving ionic and electronic conductivity, thus significantly enhancing redox kinetics. Furthermore, synergistic hydrogen bonding between FA and residual water molecules stabilizes the layered structure [43,44], ensuring superior cycling stability.

The resulting FA-intercalated $VOPO_4$ material exhibits exceptional electrochemical performance. At a mass loading of 7 mg/cm^2, FA-$VOPO_4$ delivers a remarkable specific mass capacity of 463 mAh/g and a volumetric capacity of 733 mAh/cm^3, approximately 8 times greater than that of $VOPO_4{\cdot}2H_2O$ electrode, outperforming similar results reported in the literature. Even at a significantly high mass loading of 20 mg/cm^2 (4.4 mAh/cm^2), the FA-$VOPO_4$ material exhibits a volumetric capacity of 535 mAh/cm^3. After 1000 cycles at a current density of 1 A/g and a mass loading of 10 mg/cm^2, the FA-$VOPO_4$ electrode retains 82.1% of its capacity (564 mAh/cm^3). This work represents a crucial step toward the development of high-energy-density AZIBs for practical applications.

2 Results and discussion

FA-$VOPO_4$ was synthesized the *in situ* intercalation of FA into $VOPO_4{\cdot}2H_2O$ through a combined hydrothermal and ultrasonic treatment, as detailed in the Electronic Supplementary Material. The structural characteristics of FA-$VOPO_4$ were investigated using a comprehensive suite of techniques. The X-ray diffraction (XRD) pattern (Fig. 1(a)) reveals a shift in the (001) diffraction peak from 11.9° to 9.4° after FA insertion, indicating an expansion of the interlayer spacing from 7.4 to 9.3 Å. This increased interlayer spacing is expected to enhance Zn^{2+} migration kinetics [45]. Fourier transform infrared (FTIR) spectra of $VOPO_4{\cdot}2H_2O$ and FA-$VOPO_4$ (Fig. 1(b)) confirm the presence of FA within the structure, as evidenced by characteristic peaks at 3320 cm^{-1} (N–H stretching), 1673 cm^{-1} (C=O stretching), 1416 cm^{-1} (C–N stretching), and 1616 cm^{-1} (O–H bending), corresponding to FA and residual H_2O molecules [46,47]. X-ray photoelectron spectroscopy (XPS) N 1s spectra (Fig. S1) further support the partial substitution of water by FA [48]. The O–H bending vibration of residual water shifts from 1616 cm^{-1} in $VOPO_4{\cdot}2H_2O$ to 1604 cm^{-1} in FA-$VOPO_4$, indicating that interlayer water forms stronger hydrogen bonds with the C=O or N−H groups of FA, resulting in a decreased O−H bond vibrational frequency [43,44]. Solid-state ^{13}C nuclear magnetic resonance (NMR) spectra (Fig. 1(c)) show a shift in the C(N)=O peak from 166.2 ppm in pure FA to 167.8 ppm in FA-$VOPO_4$, attributed to hydrogen bonding

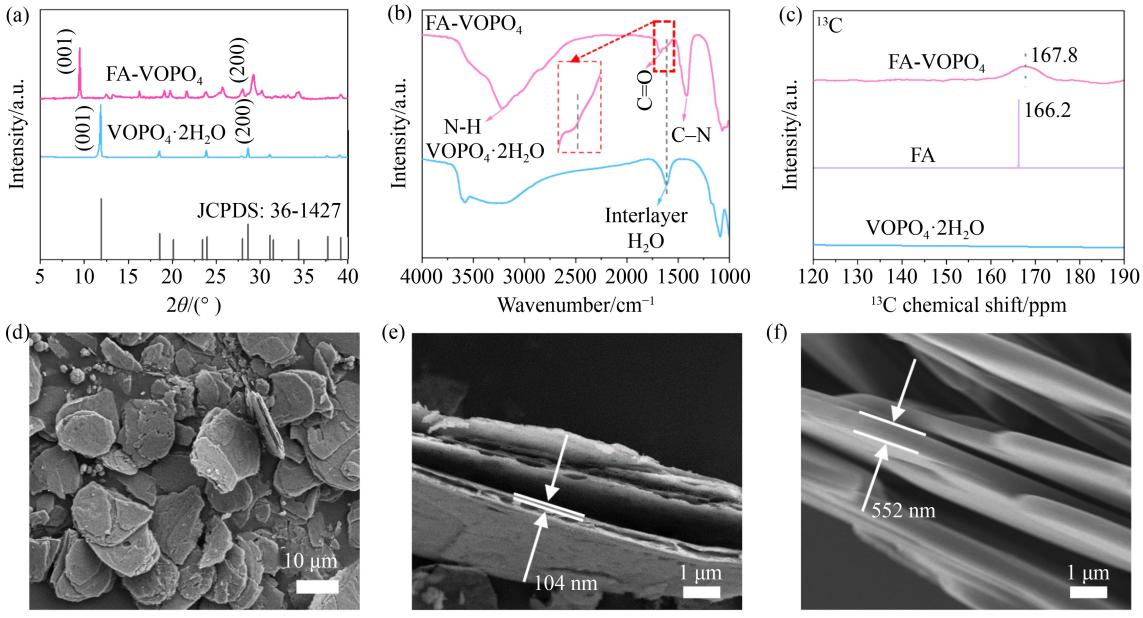

Fig. 1 Structure characterizations of FA-$VOPO_4$.

(a) XRD pattern of FA-$VOPO_4$; (b) FTIR spectra; (c) ^{13}C NMR spectra of FA-$VOPO_4$; (d) and (e) SEM image showing the morphology of FA-$VOPO_4$; (f) SEM image showing the morphology of $VOPO_4{\cdot}2H_2O$.

interactions between FA and residual water molecules.

Microscopic morphology characterized using scanning electron microscopy (SEM) (Figs. 1(d)–1(f)), reveals that the FA-$VOPO_4$ nanosheets (~104 nm) are thinner than those of $VOPO_4{\cdot}2H_2O$ (~552 nm) (Fig. S2). High-resolution transmission electron microscopy (HRTEM) images (Fig. S3) display clear lattice fringes corresponding to the (001) and (200) crystal planes, consistent with XRD results. Energy dispersive X-ray spectroscopy (EDS) mapping (Fig. S4) confirms the uniform distribution of carbon, nitrogen, oxygen, vanadium, and phosphorus throughout the nanosheets, indicating homogeneous incorporation of FA within the structural framework.

The expanded interlayer spacing in FA-$VOPO_4$ facilitates rapid zinc-ion insertion and extraction, even under high mass loading conditions. As shown in Figs. 2(a) and S5, the FA-$VOPO_4$ cathode with a mass loading of 7 mg/cm^2, delivers a high specific capacity of 463 mAh/g (733 mAh/cm^3) at 0.02 A/g, along with excellent rate capability, maintaining a specific capacity of 386 mAh/g at 0.4 A/g. This performance significantly surpasses that of $VOPO_4{\cdot}2H_2O$, which exhibits only 85 mAh/g (83 mAh/cm^3) at 0.02 A/g, approximately one-eighth the volumetric capacity of FA-$VOPO_4$ (refer to Fig. S6 for details). As the FA-$VOPO_4$ mass loading increases from ~4 mg/cm^2 to ~20 mg/cm^2, the areal capacity rises from 1.3 to 4.4 mAh/cm^2, while the volumetric capacity improves from 403 to 535 mAh/cm^3 (Figs. 2(b), S7 and S11; volumetric capacity calculation detailed in Fig. S8), meeting commercial benchmarks of 3–5 mAh/cm^2 while maintaining excellent volumetric energy density retention.

The observed decrease in specific capacity at higher loadings is attributed to the increased electron and ion transport distances in thicker electrodes. Notably, the FA-$VOPO_4$ cathode with a mass loading of 10 mg/cm^2 exhibits outstanding long-term cycling performance, retaining a volumetric capacity of 478 mAh/cm^3 after 1000 cycles at 1 A/g, with an average Coulombic efficiency (CE) of 99.95% (Fig. 2(e)). In stark contrast, $VOPO_4{\cdot}2H_2O$ undergoes rapid degradation, retaining only 31.9% of its initial capacity after 784 cycles under the same conditions. Remarkably, FA-$VOPO_4$ also demonstrates robust cycling stability under various rates and high mass loadings, retaining 85.6% of its initial capacity after 600 cycles at 0.5 A/g and 82.1% after 2000 cycles at 2 A/g, with a high mass loading of 10 mg/cm^2 (Figs. S9 and S10). Furthermore, even at an exceptionally high mass loading of 19.78 mg/cm^2 (Fig. S11), FA-$VOPO_4$ maintains remarkable cycling stability, outperforming other cathode materials reported in the literature (Table S2).

In this study, the $VOPO_4$ cathode material exhibited a gradual increase in capacity during electrochemical charge/discharge cycling. To investigate the underlying reaction mechanism, in-depth electrochemical experiments and analyses were conducted. Differential capacitance (dQ/dV) plots (Figs. 3(a) and 3(b), S12(b) and S12(c)) indicate similar electrochemical behavior for both $VOPO_4$ materials during cycling. Four pairs of redox peaks were initially observed at 1.4/1.6, 1.1/1.3, 0.8/1.1, and 0.5/0.7 V. As cycling progressed, the redox peaks at 1.4/1.6 V and 1.1/1.3 V gradually diminished, while those at 0.5/0.7 and 0.8/1.1 V became more

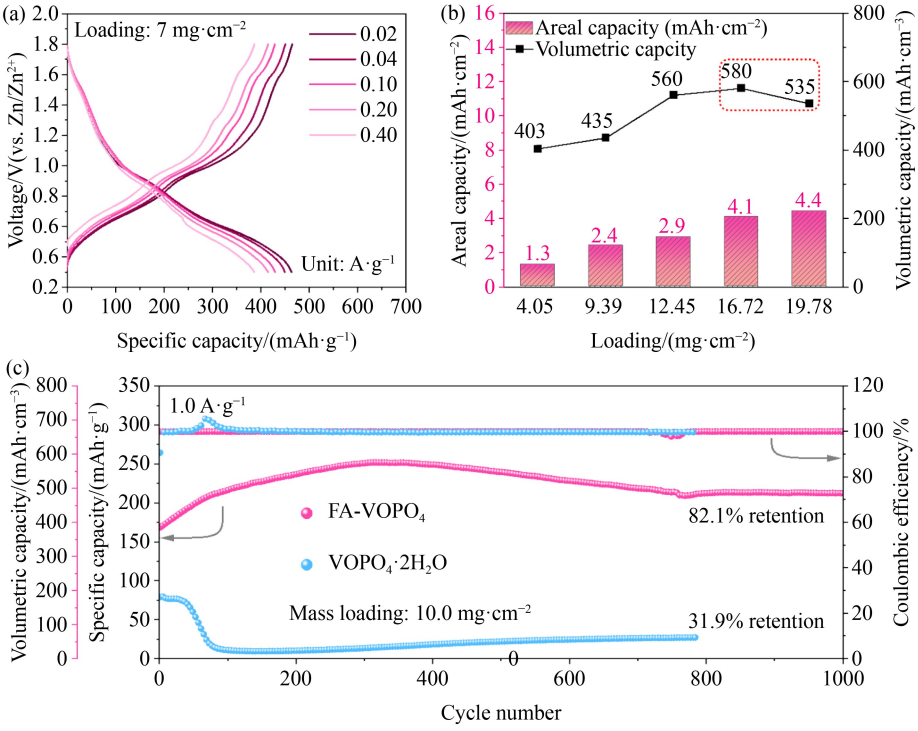

Fig. 2 Electrochemical characteristics of FA-$VOPO_4$ electrodes.

(a) Galvanostatic charge–discharge profiles for FA-$VOPO_4$ electrode at different current densities; (b) volumetric/areal capacities of FA-$VOPO_4$ cathodes with different mass loadings at 0.5 A/g; (c) long cycle capacity of FA-$VOPO_4$ with a high mass loading of 10 mg/cm^2 at 1 A/g.

pronounced. This evolution is attributed to the progressive dissolution of PO_4^{3-} and the structural transformation of $VOPO_4$ into vanadium oxides (VO_x) [28,29].

Unlike $VOPO_4{\cdot}2H_2O$, which exhibits a steady decline in electrochemical activity characterized by the fading of all redox peaks, FA-$VOPO_4$ retains high electrochemical activity even after transitioning into VO_x. Following this transformation, the FA-$VOPO_4$ cathode achieved a capacity of 303 mAh/g, significantly surpassing $VOPO_4{\cdot}2H_2O$, which retained only 42 mAh/g (Fig. 3(b)).

The phase transformation of FA-$VOPO_4$ and $VOPO_4{\cdot}2H_2O$ during cycling was systematically characterized using XRD and EDS. As shown in Fig. S13(a), the initial P/V atomic ratios of pristine $VOPO_4{\cdot}2H_2O$ and FA-$VOPO_4$ electrodes were 0.92 and 0.88, respectively. After 100 cycles in 2 mol/L $Zn(OTf)_2$ electrolyte, these ratios decreased to 0.05 ($VOPO_4{\cdot}2H_2O$) and 0.03 (FA-$VOPO_4$), indicating significant structural decomposition. XRD patterns (Fig. S13(b)) confirm the formation of $V_2O_5{\cdot}H_2O$ in both materials, consistent with previous reports describing the conversion of $VOPO_4$ into vanadium oxides during cycling. Additionally, surface characterization of the cycled electrodes (Fig. S13(b)) revealed minor formation of $Zn_3(PO_4)_2(H_2O)_4$, attributed to surface phosphate-zinc interactions, while analyzing $V_2O_5{\cdot}H_2O$ remained the dominant phase (see Fig. S13(b) and S13(c) for detailed depth profiling and EDS results).

To further elucidate the ion storage mechanism in FA-$VOPO_4$, *ex-situ* XRD and XPS analyses were performed. As shown in Figs. 3(c) and 3(d), the (200) diffraction peak of FA-$VOPO_4$ shifted to lower angles (28–30°) during discharge, indicating interlayer expansion due to H^+/Zn^{2+} insertion [49]. Upon charging, the peak returned to its original position, demonstrating excellent structural reversibility. This observation was further corroborated by *ex-situ* XPS analysis (Fig. 3(e)), which showed a reversible change in the vanadium shifted valence state from mixed V^{4+}/V^{5+} to V^{3+}/V^{4+} during discharge due to H^+/Zn^{2+} intercalation. Upon recharging, the valence state reverted to its initial configuration. Simultaneously, Zn 2p spectra (Fig. 3(f)) showed the reversible appearance and disappearance of zinc ion signals, confirming the reversible Zn^{2+} insertion/extraction process.

The ion storage characteristics in FA-$VOPO_4$ electrodes were investigated through dynamic analysis using cyclic voltammetry (CV) at scan rates ranging from 0.2 to 1.0 mV/s. The FA-$VOPO_4$ cathode exhibited similar CV curve profiles across varying scan rates, indicating minimal polarization voltage (Fig. 4(a)). As the scan rate increased, the area enclosed by the CV curves expanded progressively, suggesting enhanced capacitive behavior. Electrochemical kinetics were evaluated using

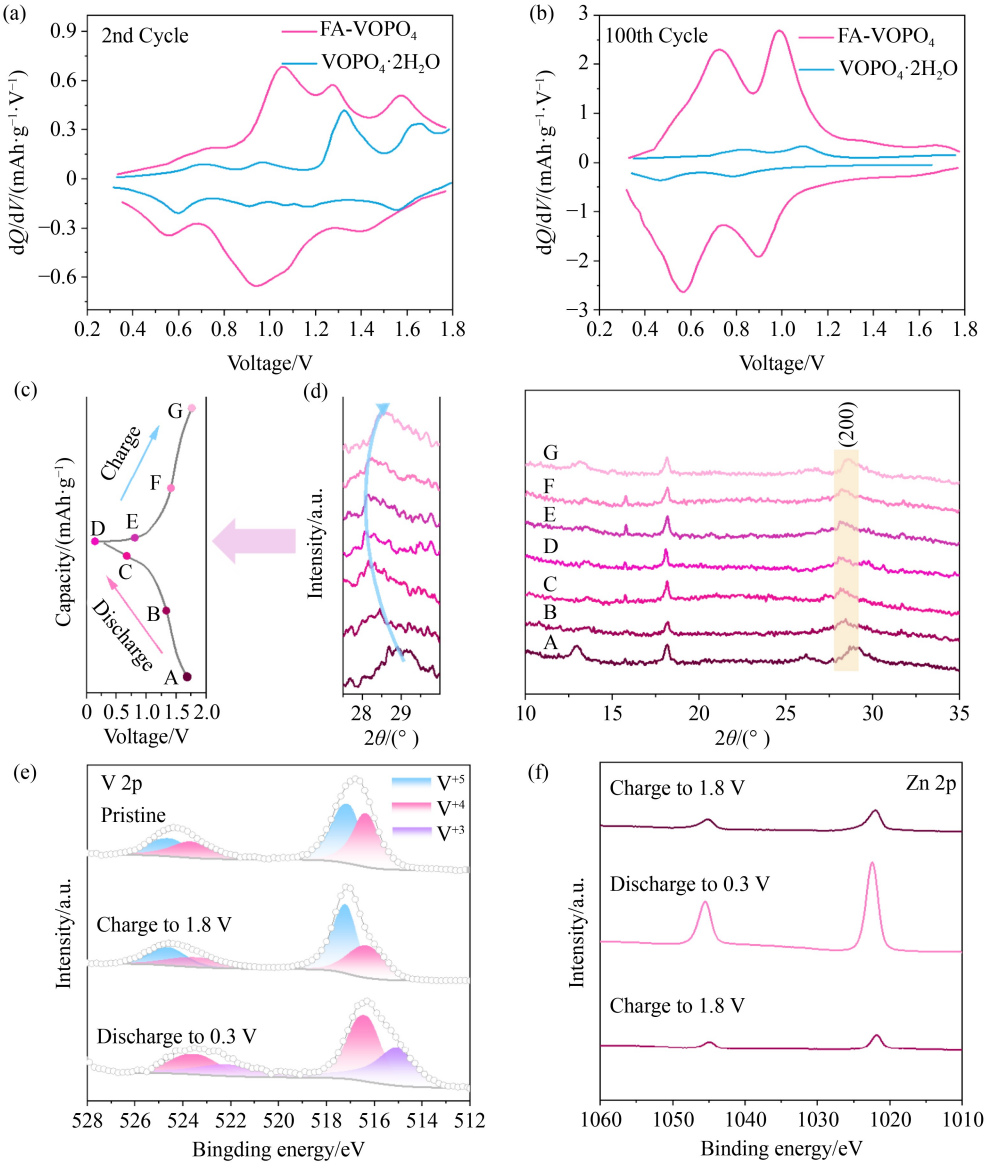

Fig. 3 H^+/Zn^{2+} charge storage mechanism analysis in aqueous electrolyte.

(a) 2nd cycle and (b) 100th dQ/dV curves of FA-$VOPO_4$ and $VOPO_4{\cdot}2H_2O$ with 2 mol/L $Zn(OTf)_2$ electrolyte; (c) GCD curve of FA-$VOPO_4$ cathode during a complete discharge–charge procedure; (d) corresponding *ex-situ* XRD patterns recorded at different voltage states; (e) *ex-situ* XPS spectrum of V 2p; (f) *ex-situ* XPS spectrum of Zn 2p.

$$i = av^b, \tag{1}$$

where i represents the peak current (mA), v is the scan rate (mV/s), a and b are fitting parameters. A b-value of 1 corresponds to a surface-controlled capacitive process, while a value near 0.5 suggests a diffusion-controlled behavior typical of faradaic reactions [50,51]. The calculated b-values for redox peaks 1 to 6 were 0.81, 0.85, 0.87, 0.98, 0.99, and 1.05, respectively (Fig. 4(b)), indicating that charge storage in FA-$VOPO_4$ is predominantly governed by capacitive behavior [52].

Ion diffusion kinetics were further explored using the galvanostatic intermittent titration technique (GITT). The Zn^{2+} diffusion coefficients ($D_{Zn}{}^{2+}$) for FA-$VOPO_4$ during both charging and discharging processes ranged from approximately 10^{-8} to 10^{-9} cm^2/s, significantly higher than those of $VOPO_4{\cdot}2H_2O$, which ranged from 10^{-9} to 10^{-10} cm^2/s (Fig. 4(c)). This improvement is attributed to the FA intercalation, which improves ion transport pathways. Electrochemical impedance spectroscopy (EIS) further revealed a significantly lower charge-transfer resistance (R_{ct}) for FA-$VOPO_4$ compared to $VOPO_4{\cdot}2H_2O$, indicating superior intrinsic electronic conductivity (Fig. 4(d); refer to Fig. S14 for details of the equivalent circuit model).

To understand the origin of the improved ion diffusion, density functional theory (DFT) calculations were performed. Zn^{2+} migration pathways were modeled using the climbing image nudged elastic band (CI-NEB)

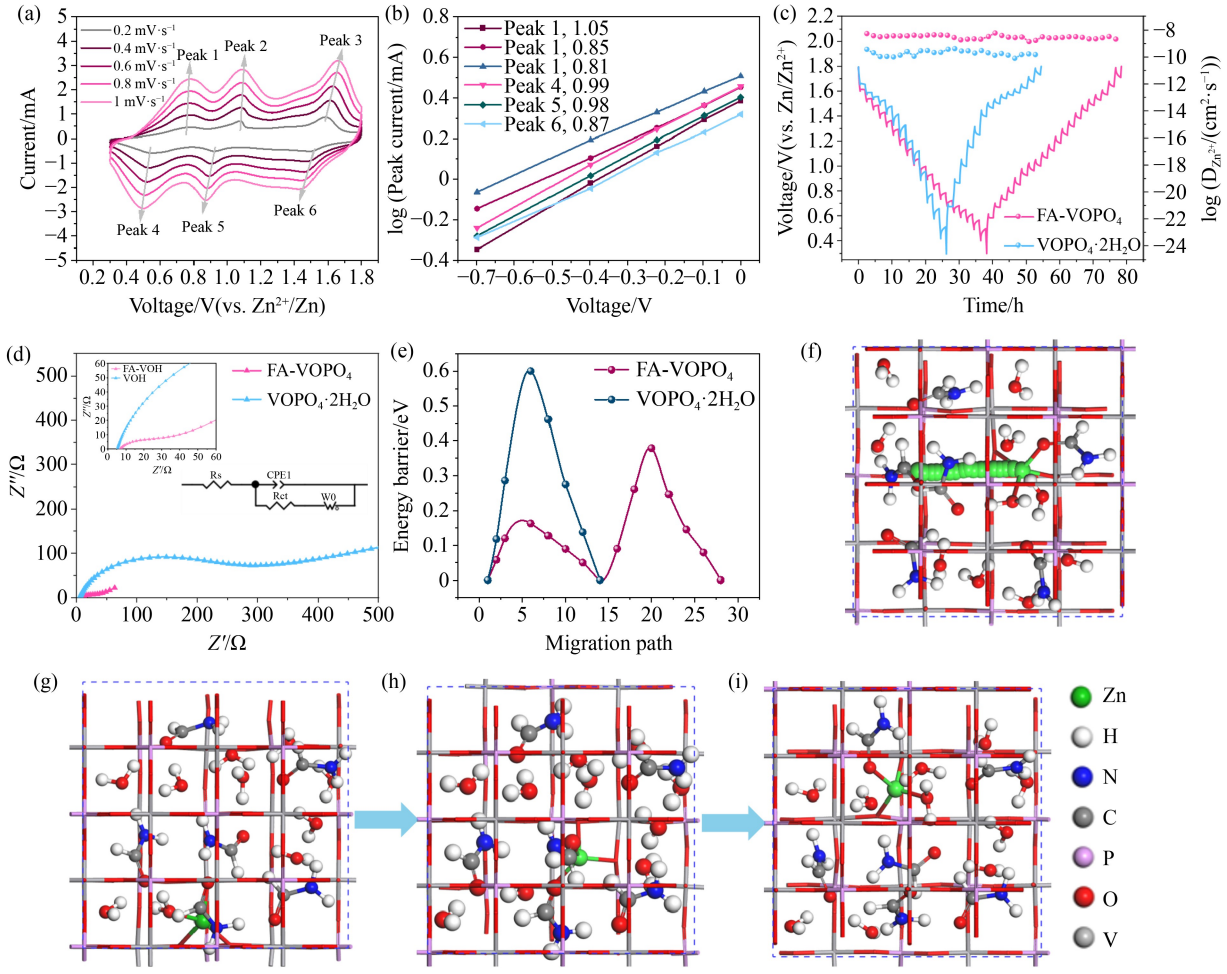

Fig. 4 Kinetics analysis of H^+/Zn^{2+} storage and calculation of Zn^{2+} diffusion barrier.

(a) CV curves with rates of 0.2–1.0 mV/s; (b) linearly fitting log*i*–log*v* plots; (c) GITT curves and calculated ion diffusion coefficients of FA-$VOPO_4$ cathode; (d) Nyquist plots of FA-$VOPO_4$ cathode; (e) calculated energy barrier curves (f)–(i) for the corresponding Zn^{2+} diffusion path schematic in top view mode of FA-$VOPO_4$ cathode.

method to calculate corresponding diffusion energy barriers (Figs. 4(e)–4(i) and S15). Intercalation of FA into $VOPO_4{\cdot}2H_2O$ induces a significant expansion of the interlayer spacing. In pristine $VOPO_4{\cdot}2H_2O$, the relatively narrow interlayer channels restrict Zn^{2+} mobility, where oxygen atoms from phosphate groups and interlayer water molecules create a complex electrostatic environment. These strong interactions with Zn^{2+} result in a high diffusion energy barrier of 0.60 eV [22,31]. The intercalation of FA into $VOPO_4{\cdot}2H_2O$ disrupts the original interlayer electrostatic field. Hydrogen bonding between FA's C=O or N–H groups and interlayer water molecules, coupled with expanded interlayer spacing, effectively alleviates electrostatic confinement, resulting in a significantly lower Zn^{2+} diffusion of 0.38 eV, markedly lower than the 0.60 eV observed in pristine $VOPO_4$.

Furthermore, FA-$VOPO_4$ demonstrates enhanced Zn^{2+} diffusion kinetics and improved electronic conductivity, supporting its excellent electrochemical performance even under high mass loading conditions.

3 Conclusions

In summary, FA-$VOPO_4$ nanosheets with enlarged interlayer spacing (9.3 Å) were successfully synthesized via a straightforward ultrasonic pulverization method. Structural characterization confirmed that FA partially replaced interlayer water molecules, leading to expanded interlayer spacing and the formation of additional Zn^{2+} migration pathways. Moreover, synergistic hydrogen bonding between FA and residual water molecules further stabilized the layered structure, contributing to excellent cyclic stability. Theoretical calculations revealed that FA intercalation significantly reduced the Zn^{2+} diffusion energy barrier, while electrochemical analysis demonstrated enhanced Zn^{2+} diffusion kinetics and enhanced electronic and ionic conductivity.

As a result, the FA-$VOPO_4$ electrode exhibited

outstanding electrochemical performance, even under high mass loading conditions. Specifically, at a mass loading of 7 mg/cm^2 and a current density of 40 mA/g, it achieved a remarkable specific capacity of 463 mAh/g and a volumetric capacity of 733 mAh/cm^3. Even at a mass loading of 20 mg/cm^2, it maintained a capacity of 535 mAh/cm^3. Long-term cycling performance further demonstrated excellent durability, with the electrode retaining 82.1% of its capacity (564 mAh/cm^3) after 1000 cycles at 1 A/g and a mass loading of 10 mg/cm^2. This study presents a significant advancement in zinc-ion battery development, offering a promising pathway toward high-energy-density, safer, and durable aqueous energy storage systems.

Acknowledgements This work was supported by the National Key Research and Development Program of China (Grant No. 2019YFA0210600), the National Natural Science Foundation of China (Grant Nos. BC0500463, 22071081, and 22461015), and the Shanghai Pilot Program for Basic Research of Shanghai Jiao Tong University, China.

Competing Interests The authors declare that they have no known competing financial interests or personal relationships that could have appeared to influence the work reported in this paper.

Electronic Supplementary Material Supplementary material is available in the online version of this article at https://doi.org/10.1007/s11708-025-1015-3 and is accessible for authorized users.

References

1. Fu Q, Zhang W, Liu X, et al. Dynamic imine chemistry enables paintable biogel electrolytes to shield on-body zinc-ion batteries from interfacial interference. Journal of the American Chemical Society, 2024, 146(50): 34950–34961
2. Wu S, Hu Z, He P, et al. Crystallographic engineering of Zn anodes for aqueous batteries. eScience, 2023, 3(3): 100120
3. Shang Y, Kundu D. A path forward for the translational development of aqueous zinc-ion batteries. Joule, 2023, 7(2): 244–250
4. Xu Y, Li T, Zhang S, et al. Compact aqueous zinc–carbon capacitors with high capacity and ultra-long lifespan. Journal of Materials Chemistry. A, Materials for Energy and Sustainability, 2024, 12(14): 8254–8261
5. Liu M, Wang P, Zhang W, et al. Strategies for pH regulation in aqueous zinc ion batteries. Energy Storage Materials, 2024, 67: 103248
6. Tang H, Chen W, Li N, et al. Layered MnO_2 nanodots as high-rate and stable cathode materials for aqueous zinc-ion storage. Energy Storage Materials, 2022, 48: 335–343
7. Xu Y, Huang W, Liu J, et al. Promoting the reversibility of electrolytic MnO_2-Zn battery with high areal capacity by $VOSO_4$ mediator. Energy & Environmental Materials, 2024, 4(1): 400005
8. Zhang F, Zhang W, Wexler D, et al. Recent progress and future advances on aqueous monovalent-ion batteries towards safe and high-power energy storage. Advanced Materials, 2022, 34(24): 2107965
9. Zhang F L, Zhang W C, Wexler D, et al. Recent progress and future advances on aqueous monovalent-ion batteries towards safe and high-power energy storage. Advanced Materials, 2022, 34(24): 2107965
10. Xu Y, Fan G, Sun P X, et al. Carbon nitride pillared vanadate via chemical pre-intercalation towards high-performance aqueous zinc-ion batteries. Angewandte Chemie International Edition, 2023, 62(26): e202303529
11. Liang W, Rao D, Chen T, et al. $Zn_{0.52}V_2O_{5-a}\cdot 1.8H_2O$ cathode stabilized by *in situ* phase transformation for aqueous zinc-ion batteries with ultra-long cyclability. Angewandte Chemie International Edition, 2022, 61(35): e202207779
12. Li C, Jin S, Archer L A, et al. Toward practical aqueous zinc-ion batteries for electrochemical energy storage. Joule, 2022, 6(8): 1733–1738
13. Zampardi G, La Mantia F. Open challenges and good experimental practices in the research field of aqueous Zn-ion batteries. Nature Communications, 2022, 13(1): 687
14. Liu Y, Li Q, Ma K, et al. Graphene oxide wrapped CuV_2O_6 nanobelts as high-capacity and long-life cathode materials of aqueous zinc-ion batteries. ACS Nano, 2019, 13(10): 12081–12089
15. Wu F, Liu M, Li Y, et al. High-mass-loading electrodes for advanced secondary batteries and supercapacitors. Electrochemical Energy Reviews, 2021, 4(2): 382–446
16. Yang L, Zhu Y J, Zeng F, et al. Synchronously promoting the electron and ion transport in high-loading $Mn_{2.5}V_{10}O_{24}\cdot 5.9H_2O$ cathodes for practical aqueous zinc-ion batteries. Energy Storage Materials, 2024, 65: 103162
17. Dandan L, Ying-Jie Z, Long C, et al. A mxene modulator enabled high-loading iodine composite cathode for stable and high-energy-density Zn-I_2 battery. Advanced Energy Materials, 2024, 15(12): 2404426
18. Ding Y, Peng Y, Chen S, et al. Hierarchical porous metallic V_2O_3@c for advanced aqueous zinc-ion batteries. ACS Applied Materials & Interfaces, 2019, 11(47): 44109–44117
19. Javed M S, Lei H, Wang Z, et al. 2d V_2O_5 nanosheets as a binder-free high-energy cathode for ultrafast aqueous and flexible Zn-ion batteries. Nano Energy, 2020, 70: 104573
20. Song Z, Zhao Y, Wang H, et al. Dual mechanism with graded energy storage in long-term aqueous zinc-ion batteries achieved using a polymer/vanadium dioxide cathode. Energy & Environmental Science, 2024, 17(18): 6666–6675
21. Zhu K, Yang W. Vanadium-based cathodes for aqueous zinc-ion batteries: Mechanisms, challenges, and strategies. Accounts of Chemical Research, 2024, 57(19): 2887–2900
22. Hu L, Wu Z, Lu C, et al. Principles of interlayer-spacing regulation of layered vanadium phosphates for superior zinc-ion batteries. Energy & Environmental Science, 2021, 14(7): 4095–4106
23. Shi H Y, Jiang Q, Wu W, et al. Assisting Zn storage in layered vanadyl phosphate cathode by interactions with oligoaniline pillars for rechargeable aqueous zinc batteries. Chemical Engineering Journal, 2023, 454: 140323
24. Wang L, Zhao M, Zhang X, et al. Novel high-voltage cathode for aqueous zinc ion batteries: Porous $K_{0.5}VOPO_4\cdot 1.5H_2O$ with

reversible solid-solution intercalation and conversion storage mechanism. Journal of Energy Chemistry, 2024, 93: 71–78
25. Xiong P, Zhang F, Zhang X, et al. Strain engineering of two-dimensional multilayered heterostructures for beyond-lithium-based rechargeable batteries. Nature Communications, 2020, 11(1): 3297
26. Jiang W, Zhu K, Yang W. Critical issues of vanadium-based cathodes towards practical aqueous Zn-ion batteries. Chemistry, 2023, 29(56): e202301769
27. Verma V, Kumar S, Manalastas W Jr, et al. Undesired reactions in aqueous rechargeable zinc ion batteries. ACS Energy Letters, 2021, 6(5): 1773–1785
28. Jia Z, Yang X, Shi H Y, et al. Stabilization of $VOPO_4{\cdot}2H_2O$ voltage and capacity retention in aqueous zinc batteries with a hydrogen bond regulator. Chemical Communications, 2022, 58(39): 5905–5908
29. Shi H Y, Jiang Q, He T, et al. Uncovering and retrieving the internal vanadium migration caused voltage fade in vanadyl phosphate cathode for aqueous zinc batteries. ACS Energy Letters, 2023, 8(12): 5215–5220
30. Wan F, Zhang Y, Zhang L, et al. Reversible oxygen redox chemistry in aqueous zinc-ion batteries. Angewandte Chemie International Edition, 2019, 58(21): 7062–7067
31. Shi H Y, Jiang Q, Wu W, et al. Assisting Zn storage in layered vanadyl phosphate cathode by interactions with oligoaniline pillars for rechargeable aqueous zinc batteries. Chemical Engineering Journal, 2023, 454: 140323
32. Verma V, Kumar S, Manalastas W Jr, et al. Layered $VOPO_4$ as a cathode material for rechargeable zinc-ion battery: Effect of polypyrrole intercalation in the host and water concentration in the electrolyte. ACS Applied Energy Materials, 2019, 2(12): 8667–8674
33. Ran Y, Ren J, Kong Y, et al. Electrochemical zinc and hydrogen co-intercalation in Li_3 (V_6O_{16}): A high-capacity aqueous zinc-ion battery cathode. Electrochimica Acta, 2022, 412: 140120
34. Zhang W, Tang C, Lan B, et al. $K_{0.23}V_2O_5$ as a promising cathode material for rechargeable aqueous zinc ion batteries with excellent performance. Journal of Alloys and Compounds, 2020, 819: 152971
35. Dilwale S, Ghosh M, Vijayakumar V, et al. Electrodeposited layered sodium vanadyl phosphate ($Na_xVOPO_4{\cdot}nH_2O$) as cathode material for aqueous rechargeable zinc metal batteries. Energy & Fuels, 2022, 36(12): 6520–6531
36. Wu Y, Zong Q, Liu C, et al. Sodium-ion substituted water molecule in layered vanadyl phosphate enhancing electrochemical kinetics and stability of zinc ion storage. Small, 2023, 19(40): 2303227
37. Jiang Y, Wu Z, Ye F, et al. Spontaneous knitting behavior of 6.7-nm thin $(NH_4)_{0.38}V_2O_5$ nano-ribbons for binder-free zinc-ion batteries. Energy Storage Materials, 2021, 42: 286–294
38. Wu Z, Lu C, Ye F, et al. Bilayered $VOPO_4{\cdot}2H_2O$ nanosheets with high-concentration oxygen vacancies for high-performance aqueous zinc-ion batteries. Advanced Functional Materials, 2021, 31(45): 2106816
39. Du Y, Wang X, Zhang Y, et al. High mass loading CaV_4O_9 microflowers with amorphous phase transformation as cathode for aqueous zinc-ion battery. Chemical Engineering Journal, 2022, 434: 134642
40. Chen S, Ji D, Chen Q, et al. Coordination modulation of hydrated zinc ions to enhance redox reversibility of zinc batteries. Nature Communications, 2023, 14(1): 3526
41. Jian Q, Wang T, Sun J, et al. Hydrated solvation suppression of zinc ions for highly reversible zinc anodes. Chemical Engineering Journal, 2023, 466: 143189
42. Jin Y Q, Chen H, Peng L, et al. Interfacial polarization triggered by glutamate accelerates dehydration of hydrated zinc ions for zinc-ion batteries. Chemical Engineering Journal, 2021, 416: 127704
43. Li M, Wang X, Meng J, et al. Comprehensive understandings of hydrogen bond chemistry in aqueous batteries. Advanced Materials, 2024, 36(3): 2308628
44. Tian Z, Guo W, Shi Z, et al. The role of hydrogen bonding in aqueous batteries: Correlating molecular-scale interactions with battery performance. ACS Energy Letters, 2024, 9(10): 5179–5205
45. Feng Z, Zhang Y, Jiang H, et al. On the origin of enhanced electrochemical kinetics in guest-ions pre-intercalated layered vanadium oxides: Interlayer spacing vs lattice distortion. Energy Storage Materials, 2024, 71: 103552
46. Räsänen M. A matrix infrared study of monomeric formamide. Journal of Molecular Structure, 1983, 101(3–4): 275–286
47. Urso R G, Scirè C, Baratta G A, et al. Infrared study on the thermal evolution of solid state formamide. Physical Chemistry Chemical Physics, 2017, 19(32): 21759–21768
48. Golczak S, Kanciurzewska A, Fahlman M, et al. Comparative xps surface study of polyaniline thin films. Solid State Ionics, 2008, 179(39): 2234–2239
49. Huang H, Xia X, Yun J, et al. Interfacial engineering of hydrated vanadate to promote the fast and highly reversible H^+/Zn^{2+} co-insertion processes for high-performance aqueous rechargeable batteries. Energy Storage Materials, 2022, 52: 473–484
50. Zhang Z, Xi B, Wang X, et al. Oxygen defects engineering of $VO_2{\cdot}xH_2O$ nanosheets via *in situ* polypyrrole polymerization for efficient aqueous zinc ion storage. Advanced Functional Materials, 2021, 31(34): 2103070
51. Zhu Q, Cai D, Lan X, et al. Design of multidimensional nanocomposite material to realize the application both in energy storage and electrocatalysis. Science Bulletin, 2018, 63(3): 152–154
52. Singh S B, Tran D T, Jeong K U, et al. A flexible and transparent zinc-nanofiber network electrode for wearable electrochromic, rechargeable Zn-ion battery. Small, 2022, 18(5): 2104462